

# Braiding Majorana corner modes in a two-layer second-order topological insulator

Tudor E. Pahomi,<sup>1,\*</sup> Manfred Sigrist,<sup>1</sup> and Alexey A. Soluyanov<sup>2,3</sup>

<sup>1</sup>*Institute for Theoretical Physics, ETH Zurich, 8093 Zurich, Switzerland*

<sup>2</sup>*Physik-Institut, University of Zurich, 8057 Zurich, Switzerland*

<sup>3</sup>*Department of Physics, St. Petersburg State University, St. Petersburg 199034, Russia*

The recent advances in the field of topological materials have established a novel understanding of material physics. Besides theoretical achievements, a number of proposals for decoherence-protected topological quantum computation were provided. It is, however, a yet unanswered question, what material could be the most feasible candidate in engineering the building blocks of a quantum computer (qubits). Here we propose a possible answer by describing a device based on a two-dimensional second-order topological insulator with particle-hole symmetry (PHS). This material has one-dimensional boundaries, but exhibits two zero-dimensional Majorana quasiparticles localized at the corners of a square-shaped sample. The two states reside at zero energy as long as PHS is conserved, whereas their corner-localization can be adjusted by in-plane magnetic fields. We consider an adiabatic cycle performed on the degenerate ground-state manifold and show that it realizes the braiding of the two zero-energy corner modes. We find that each zero-mode accumulates a non-trivial statistical phase  $\pi$  within a cycle, which confirms that, indeed, PHS ensures non-Abelian Majorana excitation braiding in the proposed device. The fractional statistics of the corner states opens the possibility to perform logical operations and, ultimately, might enable building robust qubits for large scale implementations. We also suggest possible paths for experimental realizations of this proposal.

**Introduction** – Topological materials currently include weakly correlated metals, insulators, and superconductors. Standard  $d$ -dimensional topological insulators and superconductors have a gapped bulk spectrum and exhibit conducting surface states in  $(d - 1)$  dimensions [1–8]. Considerations of non-interacting electrons in materials possessing fundamental symmetries – time-reversal symmetry (TRS,  $\mathcal{T}$ ), particle-hole symmetry (PHS,  $\mathcal{P}$ ) and/or chiral symmetry (CS,  $\mathcal{C}$ ) – led to the initial classifications of possible topological phases [9–11]. Later on, it was realized that discrete crystalline symmetries allow for a significant expansion of the list of possible topological crystalline phases [12–24]. Furthermore, investigations on materials with crystalline symmetries has recently lead to the discovery of another class of exotic non-interacting topological phases, namely the second-order topological insulators (SOTIs) and superconductors [25–40]. The gapped topological materials in this class have  $(d - 1)$ -dimensional surfaces, but host topologically-protected boundary modes in  $(d - 2)$  dimensions.

One of the main motivations in seeking for topological materials is their potential implementation in quantum devices, which would exploit the topology-ensured protection from decoherence. One such device, considered to be the cornerstone of quantum technology, is the *topological quantum computer*, in which logical operations are done by means of braiding (double exchange) of non-Abelian quasiparticle excitations [41–45]. Majorana excitations (zero-energy modes) are known to be the only non-Abelian quasiparticles that can appear in the absence of electron-electron interactions [46, 47]. Majorana quasiparticles were initially predicted to appear at the edges of a one-dimensional spinless superconductor [41]. Almost a decade later, it was proved that such an exotic topological phase could be achieved in a semiconductor nanowire with strong spin-orbit coupling (SOC) placed in an external

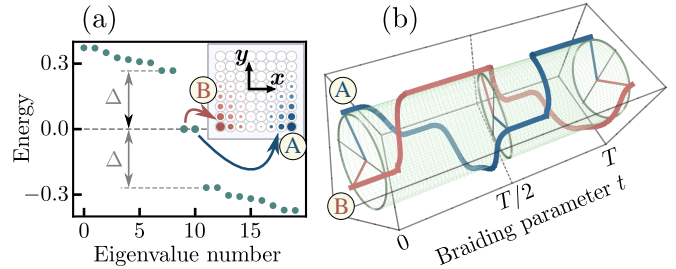


Figure 1. (a) Energy of the lowest 20 eigenstates in a finite square-shaped sample of our second-order topological insulator  $\mathcal{H}$  for parameters  $\mathbf{b} = (-0.3, 0)$  and  $\mathbf{s} = (0, 0.3)$ ; the two zero-energy modes, denoted by A and B, are separated from the bulk states by an energy gap  $\Delta$  and the probability densities  $|\psi_\alpha(x, y)|^2$  are schematically shown in the inset ( $\alpha \in \{A, B\}$ ). (b) Worldlines of A and B during the proposed cyclic adiabatic process of period  $T$ , computed as  $\arg \max_\varphi |\psi_\alpha(\varphi)|^2$  for each  $t \in [0, T]$ , with  $\varphi$  the polar angle.

magnetic field aligned with the wire, if superconductivity is induced by proximity to an  $s$ -wave superconductor [48, 49]. Following these theoretical proposals, such devices were experimentally realized by several groups [50–55] and these systems are currently considered to be the most promising basis for topological quantum computing devices.

However, despite the existing proposals of braiding Majorana end modes using such wires [56, 57], the problem of identifying the topological qubit remains extremely challenging due to the engineering complexity of manipulating the topological phase in the wire junctions without losing the topological superconducting phase. This motivates the search for other approaches to realize a Majorana qubit in an experimentally feasible condensed matter system [58–62].

Here we propose a device based on a two-dimensional (2D) crystalline SOTI composed of two coupled layers, where the presence of PHS allows for the existence of two Majorana zero-energy modes. They are localized at separate corners of

\* pahomit@phys.ethz.ch

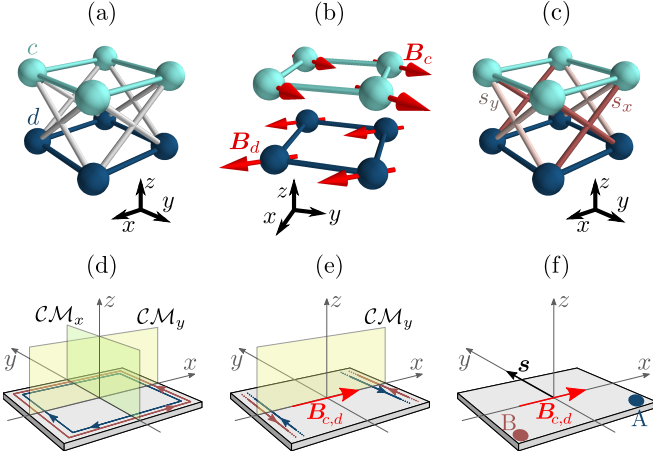


Figure 2. (a-c) Square lattice with  $2 \times 2$  unit cells, composed of two layers, with  $c$ - and  $d$ -type atoms, respectively. In panel (a) the inter- and intra-layer bonds described by  $\mathcal{H}_0$  are represented, panel (b) shows the in-plane magnetic fields  $\mathbf{B}_{c,d} = (0.16, \pm 0.25, 0)$  introduced by  $\mathcal{H}_B$  and in panel (c) the inter-layer spin-orbit coupling described by  $\mathcal{H}_s$  are displayed, with strengths  $s_x$  and  $s_y$  in  $\hat{x}$ - and  $\hat{y}$ -directions, respectively. (d) Schematic diagram for the helical state with two counter-propagating edge modes of opposite spins. At the  $x$  ( $y$ ) boundary, they are protected by the mirror antisymmetry  $CM_y$  ( $CM_x$ ), a product of chiral symmetry and the mirror reflection  $\mathcal{M}_y$  ( $\mathcal{M}_x$ ). (e) The magnetic fields  $\mathbf{B}_{c,d} = (0.3, 0, 0)$  break the mirror antisymmetry  $CM_x$  and gap the  $y$  edges. Note that  $CM_y$  does not affect  $\mathbf{B}_{c,d}$  in this case, since the effect of time-reversal symmetry (inside  $C$ ) compensates the effect of the improper rotation  $\mathcal{M}_y$ . (f) If, additionally, the parameter  $s = (0, s_y) \parallel \hat{y}$  is non-vanishing, the Hamiltonian  $\mathcal{H}_s$  breaks the  $CM_y$  antisymmetry and two zero-energy modes appear, localized at the corners (denoted by A and B).

a finite square-shaped crystalline sample (see Fig. 1a) and will be referred further as Majorana corner states (MCSs). Within our model, the localization of the MCSs in the device can be adiabatically tuned using in-plane magnetic fields, such that the corner-localization of MCSs is kept under control. In this setup, the braiding of the Majorana quasiparticles can be realized in a straightforward fashion (schematically illustrated in Fig. 1b), and below we show that the associated non-Abelian statistics of the proposed topological Majorana qubit is observed.

**SOTI model** – In  $\mathbf{k}$ -space, our proposed model can be illustrated with the minimal four-band Bloch Hamiltonian of a two-layer system  $\mathcal{H}(\mathbf{k}) = \mathcal{H}_0(\mathbf{k}) + \mathcal{H}_B + \mathcal{H}_s(\mathbf{k})$ , where the terms are:

$$\begin{aligned} \mathcal{H}_0 &= t_0(1 - \cos k_x - \cos k_y)\sigma_0\tau_3 + \\ &\quad + t_0(\sin k_x\sigma_3\tau_1 + \sin k_y\sigma_0\tau_2), \\ \mathcal{H}_B &= b_x\sigma_1\tau_0 + b_y\sigma_2\tau_3, \quad \mathcal{H}_s = (s_x \cos k_x + s_y \cos k_y)\sigma_1\tau_1. \end{aligned} \quad (1)$$

Here, the basis is set to be  $\hat{\Psi}_{\mathbf{k}} = (c_{k\uparrow} \ d_{k\uparrow} \ c_{k\downarrow} \ d_{k\downarrow})^T$ , where  $c_{k\sigma}^\dagger$  ( $d_{k\sigma}^\dagger$ ) is the creation operator for an electron in the upper (bottom) layer with a two-dimensional momentum  $\mathbf{k}$  and a spin projection  $\sigma = \pm 1$ . The two sets of Pauli matrices,  $\{\sigma_j\}$  and  $\{\tau_j\}$  with  $j \in \{0, 1, 2, 3\}$ , represent the spin and layer de-

grees of freedom, respectively, and the vectors  $\mathbf{b} \equiv (b_x, b_y)$ ,  $\mathbf{s} \equiv (s_x, s_y)$  have magnitudes smaller than  $t_0$ , which we set to be  $t_0 = 1$  in the following. The Hamiltonian terms in real-space are discussed in Appendix A.

In  $\mathcal{H}_0$ , the first term (with  $\sigma_0\tau_3$ ) accounts for the intra-layer nearest-neighbor hopping on a square lattice, while the other two terms introduce anti-symmetric inter-layer SOC (see Fig. 2a). The Hamiltonian  $\mathcal{H}_0$  possesses all three non-crystalline symmetries mentioned above ( $\mathcal{T}$ ,  $\mathcal{P}$  and  $C$ ) and falls into the symmetry class DIII [9–11], supporting helical Majorana edge states (Fig. 2d). Including crystalline symmetries, the total point symmetry group is  $\mathcal{G}_{\mathcal{H}_0} = D_{4h} \times \{\mathbb{1}, \mathcal{T}, \mathcal{P}, C\}$ , where  $\mathbb{1}$  represents the identity element. This can be written more conveniently as  $\mathcal{G}_{\mathcal{H}_0} = \tilde{\mathcal{G}}_{\mathcal{H}_0} \times \{\mathbb{1}, \mathcal{P}\}$ , where the magnetic group reads  $\tilde{\mathcal{G}}_{\mathcal{H}_0} = D_{4h} \oplus \mathcal{T} D_{4h}$  (or  $4/mmm1'$ ). More details about the symmetries of the Hamiltonian are given in Appendix B.

The second part of the Hamiltonian,  $\mathcal{H}_B$ , represents local, in-plane, layer-dependent magnetic fields, oriented as  $\mathbf{B}_{c,d} = (b_x, \pm b_y, 0)$  within the  $c$  and  $d$  layer, respectively (Fig. 2b). The magnetic fields do not affect  $\mathcal{P}$ , but break  $\mathcal{T}$  and reduce the crystalline symmetry group. The magnetic group becomes  $\tilde{\mathcal{G}}_{\mathcal{H}_0+\mathcal{H}_B} = C_{2h} \oplus \mathcal{T}(D_{2h} - C_{2h})$ <sup>1</sup> when  $\mathbf{B}_{c,d}$  are parallel to  $\hat{x}$ ,  $\hat{y}$  or  $\hat{x} \pm \hat{y}$ , and  $C_i \oplus \mathcal{T}(C_{2h} - C_i)$  otherwise (i.e.  $m'm'm$  and  $2'/m'$ , respectively). The magnetic fields hybridize the boundary modes of  $\mathcal{H}_0$  unless they are protected by symmetry: as illustrated in Fig. 2e, for  $\mathbf{b} \parallel \hat{x}$  only the  $x$  edges are still metallic because the counter-propagating states are protected by  $CM_y \in \mathcal{G}_{\mathcal{H}_0+\mathcal{H}_B}$ , a product of CS and the mirror reflection  $\mathcal{M}_y$  which maps  $(x, y, z) \mapsto (x, -y, z)$ . On the other hand, for  $\mathbf{b} \parallel \hat{y}$  the conducting states at the  $y$  edges are protected by  $CM_x$  (see Appendix C for a proof). Both edges are gapped for generic orientations  $\mathbf{b} \nparallel \hat{x}, \hat{y}$ , but, if  $\mathbf{b} \parallel (\hat{x} \pm \hat{y})$ , the mirror-symmetric corners bisected by one of the diagonals will host zero-energy modes [28, 64].

The final term,  $\mathcal{H}_s$ , represents an even-parity SOC, which induces an inter-layer spin-flipping exchange with different strength in the  $x$  and  $y$  directions (depicted in Fig. 2c). This term reduces the symmetry of  $\mathcal{H}_0+\mathcal{H}_B$  further and, in the least symmetric case we consider,  $\tilde{\mathcal{G}}_{\mathcal{H}} = C_1 \oplus \mathcal{T}(C_s - C_1)$  ( $m'$ ). This means that the (minimal) total group is  $\mathcal{G}_{\mathcal{H}} = \{\mathbb{1}, \mathcal{T}\mathcal{M}_z\} \times \{\mathbb{1}, \mathcal{P}\}$  and two elements are of particular importance,  $\mathcal{P}$  and the effective chiral symmetry  $\tilde{C} = CM_z = \mathcal{P}\mathcal{T}\mathcal{M}_z$ , which transform the Hamiltonian in the following way:

$$\mathcal{H}(\mathbf{k}) = -U_{\mathcal{P}} \mathcal{H}(-\mathbf{k})^* U_{\mathcal{P}}^\dagger \quad U_{\mathcal{P}} = \sigma_3\tau_1 \quad (2a)$$

$$\mathcal{H}(\mathbf{k}) = -U_{\tilde{C}} \mathcal{H}(\mathbf{k}) U_{\tilde{C}}^\dagger \quad U_{\tilde{C}} = \sigma_2\tau_1 \quad (2b)$$

**Majorana corner states** – Because the total Hamiltonian is  $\mathcal{P}$ -symmetric, it hosts zero-energy Majorana excitations; their features in the second-order topological phase are displayed in Fig. 1a for  $\mathbf{b} = (-0.3, 0)$  and  $\mathbf{s} = (0, 0.3)$ . In this regime,

<sup>1</sup> Here, the set  $(D_{2h} - C_{2h})$  represents the relative complement of  $C_{2h}$  with respect to  $D_{2h}$ . It contains the elements of  $D_{2h}$  which are not part of  $C_{2h}$  and it is *not* a group by itself.

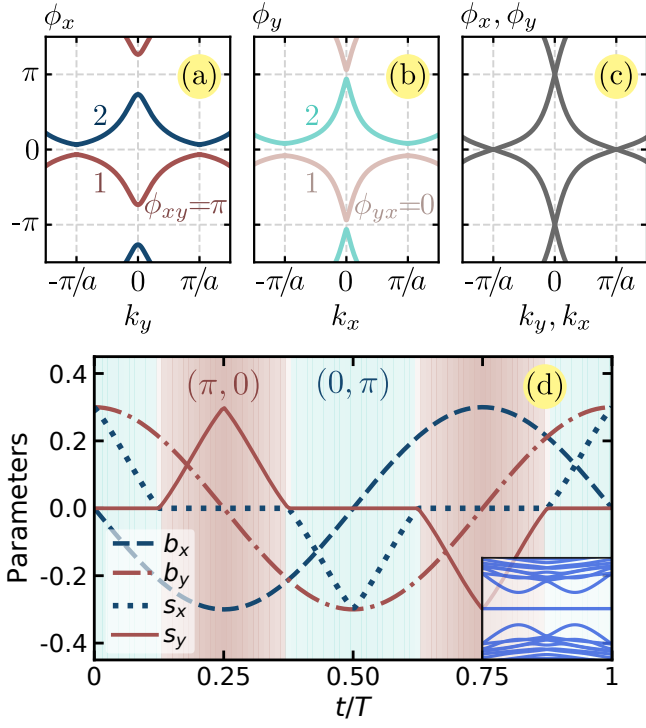


Figure 3. Non-Abelian Berry phases  $\phi_x^n$  (a) and  $\phi_y^n$  (b), with  $n \in \{1, 2\}$  indicated on each panel, for the second-order topological insulator  $\mathcal{H}$  with parameters  $\mathbf{b} = (-0.3, 0)$  and  $\mathbf{s} = (0, 0.3)$ . The second-order Berry phase of the “occupied” band  $\phi_x^1(k_y)$  in panel (a) is  $\phi_{xy} = \pi$ , while the flow  $\{\phi_y^n(k_x)\}$  in panel (b) is trivially gapped:  $\phi_{yx} = 0$ . Panel (c) shows the non-Abelian Berry phases [either  $\phi_x^n(k_y)$  or  $\phi_y^n(k_x)$ ] for the bare Hamiltonian  $\mathcal{H}_0$ , i.e. parameters  $\mathbf{b} = \mathbf{s} = (0, 0)$ . In this case, the lack of the gap in the spectrum reflects the metallic character of all edges in the helical state. (d) The evolution of the Hamiltonian parameters  $\mathbf{b} \equiv (b_x, b_y)$  and  $\mathbf{s} \equiv (s_x, s_y)$  during the cyclic adiabatic process of period  $T$ . The alternating dark-light background colors correspond to second-order topological phases with invariants  $(\phi_{xy}, \phi_{yx}) = (\pi, 0)$  or  $(0, \pi)$ , respectively; for the former case, the non-Abelian Berry phases are given in panels (a-b) at  $t = T/4$ . The inset displays the energy eigenvalues of the finite lattice in the range  $E \in [-0.4, 0.4]$ , during the last quarter of the cyclic process (the period of the eigenvalues is  $T/4$ ), and proves the energy of the Majorana states remains zero.

although the magnetic fields  $\mathbf{B}_{c,d} \parallel \hat{\mathbf{x}}$  would allow for  $C\mathcal{M}_y$ -protected boundary modes at the  $x$  edges, the inter-layer hopping term  $\mathcal{H}_s$  gaps the  $x$  edges by breaking this symmetry (Fig. 2f) and enforces the zero-energy modes to localize at the bottom corners of the device (as shown in the inset of Fig. 1a). Indeed,  $\mathcal{H}_s$  reduces  $\tilde{\mathcal{G}}_{\mathcal{H}_0 + \mathcal{H}_B} = C_{2h} \oplus \mathcal{T}(D_{2h} - C_{2h})$  to  $\tilde{\mathcal{G}}_{\mathcal{H}} = C_s \oplus \mathcal{T}(C_{2v} - C_s)$  (i.e.  $m'm'm$  to  $m'm'2'$ ) and the only purely crystalline symmetry of  $\tilde{\mathcal{G}}_{\mathcal{H}}$ ,  $\mathcal{M}_x$ , can be observed in the electron density profile.

The energies of the midgap states go to zero exponentially with system size and are well separated from the bulk states by an energy gap (emphasized in Fig. 1a and discussed in Appendix A). The localization of the boundary modes is strongly dependent on the Hamiltonian parameters  $\mathbf{b}$  and  $\mathbf{s}$ , whereas their energy remains zero for all the considered configura-

tions, in which the device is in a SOTI phase. This degenerate ground state manifold is crucial to realizing the braiding of the topological zero-energy modes.

*Computing topological invariants* – We assess the topological state of our device by taking advantage of a robust algorithm that involves only reciprocal space calculations. The central role is played by the Wilson loop operator (WLO), which firstly allows us to analyze the edge topology and then, in some sense “iteratively,” to understand the topology at “the end of the edge”. A more detailed presentation of this technique, based on the works of Refs. [25, 26], can be found in Appendix D.

The operator which characterizes the  $x$  boundary is the WLO [65–67] in  $\hat{\mathbf{x}}$ -direction:

$$\mathcal{W}_{x,k} = \exp\left(i \oint_{q_y=k_y} dq_x \mathcal{A}_q^x\right), \quad (3)$$

where the  $N_{\text{occ}} \times N_{\text{occ}}$  matrix  $\mathcal{A}_k^x$  represents the  $x$ -th component of the non-Abelian Berry connection [68, 69] constructed with the occupied bands of the Hamiltonian ( $N_{\text{occ}} = 2$  here) and the integral is computed for fixed  $q_y = k_y$  along a closed loop in the Brillouin zone, in  $q_x$ -direction.

The WLO can be adiabatically connected to the Hamiltonian at the boundary [70, 71], which makes it a reliable tool for characterizing the surface topology of materials, such as  $\mathbb{Z}_2$  topological (crystalline or not) insulators in 2D and 3D [3, 66, 71–76] or  $\mathbb{Z}$  Chern insulators [65, 67, 74, 76]. For this reason, we refer to  $\mathcal{W}_{x,k}$  as “the edge Hamiltonian”<sup>2</sup>. Its spectrum depends only on  $k_y$  and, within our model, it consists of  $N_{\text{occ}} = 2$  bands  $\{\phi_x^n(k_y)\}_{n=1,2}$ . The bands do not touch each other in the whole interval  $k_y \in [0, 2\pi]$  (see Fig. 3a and a more detailed analysis in Appendix D), which indicates that the corresponding  $x$  boundaries are insulating. The single “occupied band” (chosen conventionally) can be topologically characterized separately by computing the WLO of  $\mathcal{W}_{x,k}$ :

$$\tilde{\mathcal{W}}_{xy,k_x} = \exp\left(i \oint_{q_x=k_x} dq_y \tilde{\mathcal{A}}_q^{xy}\right). \quad (4)$$

The above operator represents the *nested* WLO introduced in the work of Ref. [25], which has been successfully used to investigate the corner physics [29, 35, 78]. Its structure resembles the WLO of Eq. (3), however, here the special Berry connection  $\tilde{\mathcal{A}}_k^{xy}$  is integrated, associated to the “occupied space” of the edge Hamiltonian  $\mathcal{W}_{x,k}$ . Since this consists of a single band (well defined when  $\phi_x^n$  present a full gap),  $\tilde{\mathcal{W}}_{xy,k_x}$  is complex number of unit magnitude (instead of a unitary matrix) and its phase can be understood a second-order Berry phase. The desired corner topological invariant sums up the contributions from all momenta:

$$\phi_{xy} = \frac{a}{2\pi} \int_0^{2\pi/a} dk_x \arg \tilde{\mathcal{W}}_{xy,k_x}. \quad (5)$$

<sup>2</sup> The Hermitian edge Hamiltonian  $H_{\text{edge}}$  could be related to the *unitary* WLO through the mapping  $\mathcal{W}_{x,k} = \exp(iH_{\text{edge}})$ .

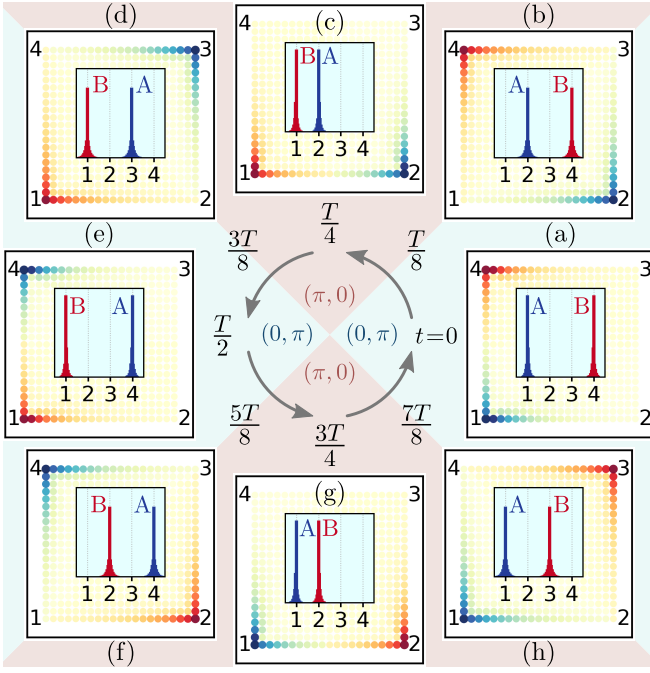


Figure 4. Square lattices with  $21 \times 21$  sites, displaying the spatial probability density  $P_A(t; x, y)$  (blue color) and  $P_B(t; x, y)$  (red color) of the two zero-modes A and B during the adiabatic cycle, at time  $t_a = 0$  in panel (a),  $t_b = T/8$  in panel (b),  $t_c = 2T/8$  in panel (c) etc. The probability of localization is maximum at the corners of the lattice (labeled with 1, 2, 3 and 4), which can be seen from the intensity of the colors. This feature is emphasized in the insets, where we used the parametrization  $(x, y) = r(\cos \varphi, \sin \varphi)$  and plotted the angular probability distributions  $P_\alpha(t; \varphi)$  for  $\alpha \in \{A, B\}$ . The background colors are alternating when  $t \in [0, T]$  and have the same meaning as in Fig. 3d: the two light cyan regions centered on  $t = 0$  and  $t = T/2$  correspond to the second-order topological phase with topological invariants  $(\phi_{xy}, \phi_{yx}) = (0, \pi)$ , whereas the two darker regions centered on  $T/4$  and  $3T/4$  correspond to  $(\pi, 0)$ .

The Hamiltonian of the perpendicular boundary ( $\mathcal{W}_{y,k}$ ), the nested WLO ( $\widetilde{\mathcal{W}}_{yx,k_y}$ ) and the corresponding corner topological invariant ( $\phi_{yx}$ ) are computed similarly, by formally exchanging the labels  $x \leftrightarrow y$  in the last three equations. In our model, the  $\mathbb{Z}_2$  topological invariants  $\phi_{xy}, \phi_{yx} \in \{0, \pi\}$  are quantized by the effective CS introduced in Eq. (2b). The device is in a SOTI phase whenever either of  $\{\phi_{xy}, \phi_{yx}\}$  is equal to  $\pi$ ; for the case  $\mathbf{b} = (-0.3, 0)$  and  $\mathbf{s} = (0, 0.3)$ , shown in Fig. 3a-b, Eq. (5) gives  $(\phi_{xy}, \phi_{yx}) = (\pi, 0)$ <sup>3</sup>.

**Braiding process** – We perform the adiabatic braiding of the MCSs by rotating the magnetic fields and adjusting the SOC ( $\mathcal{H}_s$ ). Let  $T$  be the time period of the cyclic process and  $t \in [0, T]$  the adiabatic parameter which controls the process; we have periodic boundary conditions  $\mathcal{H}^{(t=0)} = \mathcal{H}^{(t=T)}$  and the evolution of the parameters  $\mathbf{b}(t)$  and  $\mathbf{s}(t)$  over a full period is shown in Fig. 3d. Along this path in parameter space,

the energy gap of the bulk Hamiltonian  $\mathcal{H}(\mathbf{k})$  remains wide open and practically constant, at  $\approx 1.4$  in the units of  $t_0$ . The boundaries are gapped as well, which is confirmed by the non-vanishing WLO gaps (exemplified in Fig. 3a-b at  $t = T/4$ ); during the braiding process, the "occupied band"  $\phi_x^1$  carries a  $\pi$  Berry phase when  $\phi_y^1$  is trivial and vice-versa, such that the second-order topological phases  $(\phi_{xy}, \phi_{yx}) = (\pi, 0)$  and  $(0, \pi)$  alternate (illustrated by the alternating background in Fig. 3d).

The energy of the degenerate midgap MCSs (labeled with  $\alpha = \{A, B\}$ ) remains unaffected during the braiding, whereas the energy of the other eigenstates is sensitive to changes in the Hamiltonian parameters (features displayed in the inset of Fig. 3d). However, the energy gap does not close, meaning that the corner states do not mix with bulk states; Fig. 4 shows the spatial probability density of the MCSs  $|\psi_\alpha(t)\rangle$  in the proposed device,  $P_\alpha(t; \mathbf{r}) := \|\langle \mathbf{r} | \psi_\alpha(t) \rangle\|^2$ , at  $t$  intervals of  $T/8$ .

**Statistical phase and conclusion** – For a system of fermions, the many-body wavefunction picks a factor  $(-1)$  upon exchanging any two fermions and it reverts to the initial wavefunction if the exchange is repeated. In contradistinction, the double exchange (braiding) of Majorana quasiparticles yields a state which differs from the initial one: a non-trivial statistical phase  $\Phi = \pi$  is acquired [42, 43, 45]. The device we propose here realizes the braiding of two zero-energy modes and their statistics is indeed that of Majorana quasiparticles.

To express the braiding phase accumulated by each of the two midgap states within one full cycle, we use the Berry phase defined as

$$\Phi_\alpha = \oint_0^T [\mathcal{A}_t]_{\alpha\alpha} dt, \quad (6)$$

where  $\alpha$  labels the two states ( $\alpha \in \{A, B\}$ ) and the Berry connection matrix has elements  $[\mathcal{A}_t]_{\alpha\beta} = i \langle \psi_\alpha(t) | \partial_t | \psi_\beta(t) \rangle$ . More details are given in Appendix E. The Berry phase in Eq. (6) is a gauge-invariant quantity because the matrix  $\mathcal{A}_t$  is diagonal  $\forall t \in [0, T]$ , as the two MCSs are kept far apart from each other and do not mix during the course of the adiabatic cycle. The null spatial overlap of the two states A and B was checked numerically for  $t \in [0, T]$  and is illustrated in Fig. 1b. With Eq. (6), we obtain non-trivial statistical phases  $\Phi_A = \Phi_B = \pi$ , or

$$\begin{cases} \psi_A & \rightarrow & -\psi_A \\ \psi_B & \rightarrow & -\psi_B \end{cases}, \quad (7)$$

which is the signature of the fractional statistics of Majorana quasiparticles [42, 43]. The quantization of the statistical phase is guaranteed by PHS, Eq. (2a).

**Experimental realization** – The catalog of realized second-order topological insulators is extremely limited at the moment and does not contain any candidate layered compound similar to the one proposed here. While further research might lead to appropriate real materials or interfaces, which would allow manipulating the SOC with optical or electric gates [80, 81], we would like to look into other possible experimental paths for realization of the proposed scheme.

<sup>3</sup> If we considered  $\mathbf{b} = (0, -0.3)$  and  $\mathbf{s} = (0.3, 0)$ , the opposite would be valid:  $(\phi_{xy}, \phi_{yx}) = (0, \pi)$ .

A possible realization of the proposed device can be reached using an artificial lattice of cold atoms, where several topological phases have already been obtained and investigated [82–84]. Within this framework, the main experimental challenge would be the implementation of the  $\mathcal{H}_s$  term, because it would involve connecting different atomic levels (corresponding to the  $c$  and  $d$  layers) with opposite spin projections that reside in adjacent unit cells.

Once this term is engineered, the proposed cyclic process could be realized by using  $\mathbf{b}(t)$  and  $\mathbf{s}(t)$  provided in Fig. 3d. In fact, small changes to the proposed  $\mathbf{b}(t)$  and  $\mathbf{s}(t)$ , that might come within the experimental implementation, are not expected to change the topological features of the cycle. While the second-order topological invariants could be assessed during the cycle by momentum-space interference [85–88], the braiding would only be confirmed by imaging the corner states in real-space. The required sharp sample boundaries could be realized by using a varying lattice potential [89] or mimicked by the natural edges of a synthetic dimension [90, 91].

**Acknowledgment** – T.E.P. would like to thank J.L. Lado, T. Kawakami and K. Viebahn for helpful discussions. T.E.P. and M.S. are grateful for the financial support from the Swiss National Science Foundation (SNSF) through Division II (No. 163186 and 184739). A.A.S. acknowledges the support of Microsoft Research, SNSF NCCR MARVEL and QSIT programs, and the SNSF Professorship grant.

### Appendix A: Hamiltonian in real space

The Hamiltonian terms are schematically represented in real space in Fig. 5. The total Hamiltonian  $\mathcal{H} = \sum_{\mathbf{k}} \hat{\Psi}_{\mathbf{k}}^\dagger \mathcal{H}(\mathbf{k}) \hat{\Psi}_{\mathbf{k}}$  reads explicitly:

$$\begin{aligned} \mathcal{H} = & \sum_{\mathbf{k}, \sigma} \left\{ \xi_{\mathbf{k}} (c_{\mathbf{k}\sigma}^\dagger c_{\mathbf{k}\sigma} - d_{\mathbf{k}\sigma}^\dagger d_{\mathbf{k}\sigma}) \right. \\ & + \left[ (\sigma \sin k_x - i \sin k_y) c_{\mathbf{k}\sigma}^\dagger d_{\mathbf{k}\sigma} + \text{H.c.} \right] \\ & + \sum_{\sigma'} \left[ c_{\mathbf{k}\sigma}^\dagger (\mathbf{B}_c \cdot \boldsymbol{\sigma})_{\sigma\sigma'} c_{\mathbf{k}\sigma'} + d_{\mathbf{k}\sigma}^\dagger (\mathbf{B}_d \cdot \boldsymbol{\sigma})_{\sigma\sigma'} d_{\mathbf{k}\sigma'} \right] \\ & \left. + (s_x \cos k_x + s_y \cos k_y) (c_{\mathbf{k}\sigma}^\dagger d_{\mathbf{k}, -\sigma} + \text{H.c.}) \right\} \end{aligned} \quad (\text{A1})$$

Here,  $\boldsymbol{\sigma} = (\sigma_1, \sigma_2, \sigma_3)$  is the vector containing the Pauli matrices, the summing indices  $\sigma$  and  $\sigma'$  take the values  $\pm 1$  for spin-up and spin-down, respectively, and H.c. is a shorthand notation for Hermitian conjugate.

We consider a square lattice with  $N$  unit cells per side. The real-space Hamiltonian is obtained through the Fourier transforms

$$c_{\mathbf{k}\sigma} = \frac{1}{N} \sum_{\mathbf{r}} e^{i\mathbf{k}\cdot\mathbf{r}} c_{\mathbf{r}\sigma}, \quad d_{\mathbf{k}\sigma} = \frac{1}{N} \sum_{\mathbf{r}} e^{i\mathbf{k}\cdot\mathbf{r}} d_{\mathbf{r}\sigma}. \quad (\text{A2})$$

We denote the lattice constant with  $a$  and the unit vectors in the  $xOy$  plane, with  $\hat{\mathbf{x}} \equiv (a, 0)$  and  $\hat{\mathbf{y}} \equiv (0, a)$ . The real-space

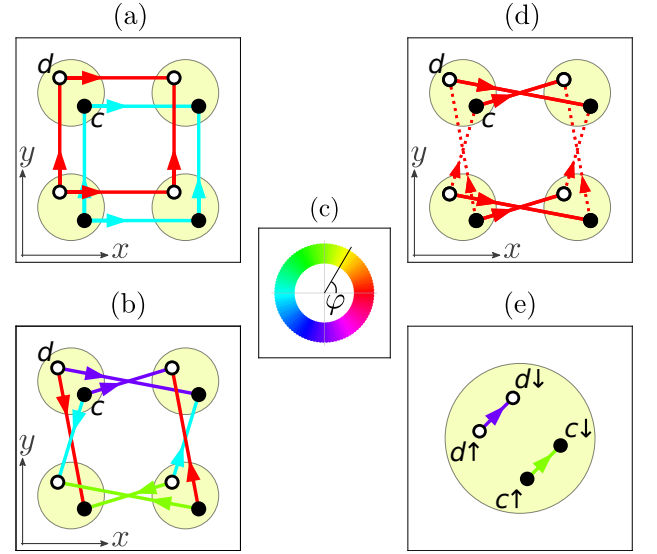


Figure 5. (a-b,d): Square lattices with  $2 \times 2$  unit cells, where a full (open) circle represents the  $c$  ( $d$ ) orbital. The links between orbitals represent schematically (a) the spin-independent intra-layer hopping corresponding to the Hamiltonian term  $(1 - \cos k_x - \cos k_y)\sigma_0\tau_3$ , (b) the spin-conserving inter-layer couplings corresponding to the term  $(\sin k_x\sigma_3\tau_1 + \sin k_y\sigma_0\tau_2)$  and (d) the inter-layer spin-flipping hopping  $s_x \cos k_x\sigma_1\tau_1$  (thick lines) and  $s_y \cos k_y\sigma_1\tau_1$  (thin lines). (e) Schematic representation of the coupling terms corresponding to  $b_y\sigma_2\tau_3$ , inside one unit cell; here, the two spin projections  $\sigma = \uparrow, \downarrow$  have been spatially separated for clarity. As suggested in panel (c), the color of the links between two orbitals  $i$  and  $j$  encodes the complex phase  $\varphi_{ij} = \arg t_{ij}$  of the real-space hopping amplitude  $t_{ij}$ .

Hamiltonian is given by

$$\begin{aligned} \mathcal{H} = & \sum_{\mathbf{r}, \sigma} \left\{ (c_{\mathbf{r}\sigma}^\dagger c_{\mathbf{r}\sigma} - d_{\mathbf{r}\sigma}^\dagger d_{\mathbf{r}\sigma}) - \frac{1}{2} \sum_{\mathbf{a} \in \{\pm\hat{\mathbf{x}}, \pm\hat{\mathbf{y}}\}} (c_{\mathbf{r}\sigma}^\dagger c_{\mathbf{r}+\mathbf{a}\sigma} - d_{\mathbf{r}\sigma}^\dagger d_{\mathbf{r}+\mathbf{a}\sigma}) \right. \\ & + \frac{1}{2} \left[ \sigma i (c_{\mathbf{r}\sigma}^\dagger d_{\mathbf{r}+\hat{\mathbf{x}}\sigma} - c_{\mathbf{r}\sigma}^\dagger d_{\mathbf{r}-\hat{\mathbf{x}}\sigma}) + (c_{\mathbf{r}\sigma}^\dagger d_{\mathbf{r}+\hat{\mathbf{y}}\sigma} - c_{\mathbf{r}\sigma}^\dagger d_{\mathbf{r}-\hat{\mathbf{y}}\sigma}) + \text{H.c.} \right] \\ & + \sum_{\sigma'} \left[ c_{\mathbf{r}\sigma}^\dagger (\mathbf{B}_c \cdot \boldsymbol{\sigma})_{\sigma\sigma'} c_{\mathbf{r}\sigma'} + d_{\mathbf{r}\sigma}^\dagger (\mathbf{B}_d \cdot \boldsymbol{\sigma})_{\sigma\sigma'} d_{\mathbf{r}\sigma'} \right] \\ & \left. + \frac{s_x}{2} \sum_{\mathbf{a} \in \{\pm\hat{\mathbf{x}}\}} (c_{\mathbf{r}\sigma}^\dagger d_{\mathbf{r}+\mathbf{a}, -\sigma} + \text{H.c.}) + \frac{s_y}{2} \sum_{\mathbf{a} \in \{\pm\hat{\mathbf{y}}\}} (c_{\mathbf{r}\sigma}^\dagger d_{\mathbf{r}+\mathbf{a}, -\sigma} + \text{H.c.}) \right\} \end{aligned} \quad (\text{A3})$$

On a finite square  $N \times N$  lattice, the model exhibits two Majorana corner states (MCSs) – see Fig. 1a or Fig. 6a-b. Their energy goes to zero exponentially with increasing  $N$ : it scales like  $\propto \exp(-N/N_0)$ , as Fig. 6c shows ( $N_0$  being a constant).

### Appendix B: Symmetries of the model Hamiltonian

Certain symmetries  $\mathcal{S} \in \mathcal{G}_{\mathcal{H}_0} = D_{4h} \times \{\mathbb{1}, \mathcal{T}, \mathcal{P}, \mathcal{C}\}$  are listed in Table I, alongside with the corresponding representations. The PHS is always present in our model, while certain symmetries involving TRS will be broken by the magnetic field

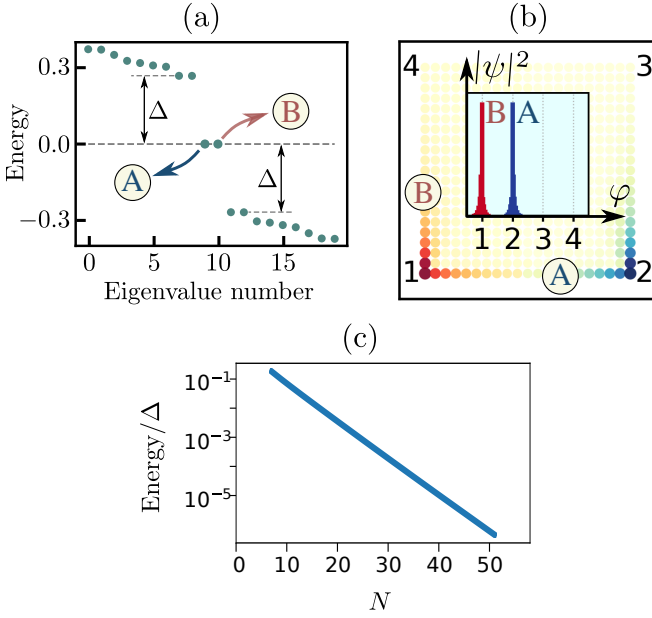


Figure 6. (a) Energy of the lowest 20 eigenstates in a square-shaped sample with  $21 \times 21$  unit cells, for Hamiltonian parameters  $\mathbf{b} = (-0.3, 0)$  and  $\mathbf{s} = (0, 0.3)$ ; there are two zero-energy modes, denoted by A and B. (b) Spatial probability density  $|\psi_A(x, y)|^2$  (blue color) and  $|\psi_B(x, y)|^2$  (red color) of the two zero-modes represented on the square lattice with  $N = 21$  cells per side. Inset: the spatial probability density of the two zero-modes as a function of the polar angle  $\varphi$ ; the four corners of the lattice, localized at  $\varphi \in \{-3\pi/4, -\pi/4, \pi/4, 3\pi/4\}$  were labeled as 1, 2, 3 and 4. (c) The energy of the zero-modes, normalized by the bulk energy gap, as a function of the linear system size ( $N$ ).

term  $\mathcal{H}_B$ . In this context, as explained in the main text, it is convenient to write

$$\mathcal{G}_{\mathcal{H}_0} = \mathcal{G}_{\mathcal{H}_0}^{\text{HS}} \times \{\mathbb{1}, \mathcal{P}\}, \quad \mathcal{G}_{\mathcal{H}_0}^{\text{HS}} = D_{4h} \oplus \mathcal{T} D_{4h}, \quad (\text{B1})$$

where  $\mathcal{G}_{\mathcal{H}_0}^{\text{HS}}$  represents the Heesch-Schubnikov magnetic group [92] of type II. When the extra terms  $\mathcal{H}_B + \mathcal{H}_s$  are introduced, the TRS is broken we obtain a magnetic group of type III:

$$\mathcal{G}_{\mathcal{H}}^{\text{HS}} = \mathcal{N} \oplus \mathcal{T}(\mathcal{G} - \mathcal{N}), \quad \mathcal{N} \triangleleft \mathcal{G} \leq D_{2h} < D_{4h}. \quad (\text{B2})$$

In Eq. (B2),  $\mathcal{G}$  represents a subgroup of  $D_{2h}$  and  $\mathcal{N}$  is a halving (and normal) subgroup of  $\mathcal{G}$ . The following relations between the subgroups of  $D_{2h}$  hold:

$$D_{2h} (mmm) > \begin{cases} C_{2v} (mm2) > C_{1h} (m) > C_1 (1) \\ C_{2h} (2/m) > C_{1h} (m) > C_1 (1) \\ C_{2h} (2/m) > C_i (\bar{1}) > C_1 (1) \end{cases} \quad (\text{B3})$$

Both  $\mathcal{G}$  and  $\mathcal{N}$  depend on the Hamiltonian parameters and are given explicitly in Table I for certain values of  $\mathbf{b}$  and  $\mathbf{s}$ ; in those six cases, the magnetic point groups  $\mathcal{G}_{\mathcal{H}}^{\text{HS}}$  in international notation read  $m'm'm'$ ,  $m'm'2'$ ,  $2'/m'$ ,  $m'$ ,  $m'm'm'$ ,  $m'm'2'$ .

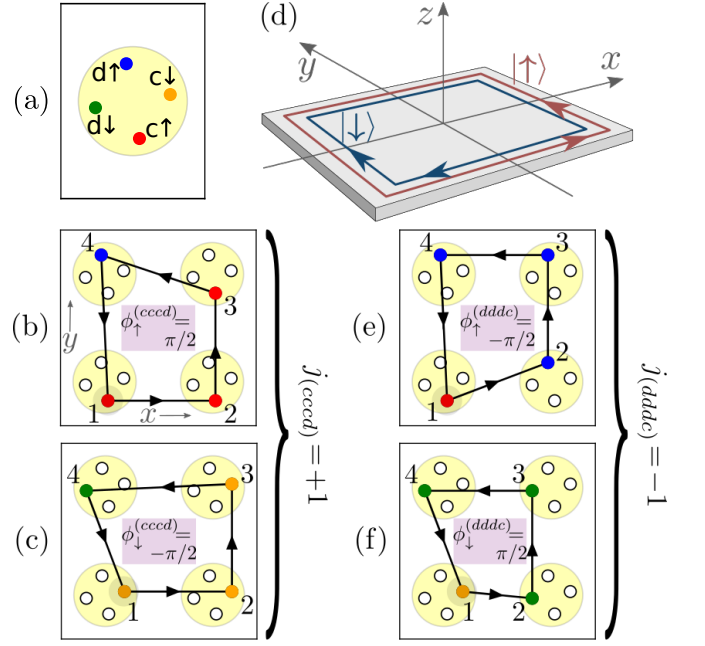


Figure 7. (a) The unit cell of the proposed model, with two kinds of orbitals ( $c$  and  $d$ ) whose spin projections  $\sigma = \uparrow, \downarrow$  are spatially separated for clarity. (b-c,e-f) Square lattices with  $2 \times 2$  such unit cells, on which four different hopping paths  $a_1 \rightarrow a_2 \rightarrow a_3 \rightarrow a_4 \rightarrow a_1$  are emphasized, where  $a_i$  can stand for either  $c$  or  $d$  orbitals with either spin projection on the unit cell  $i$ . Along this closed paths, the total phase accumulated from the four terms  $t_i a_i^\dagger a_{i+1}$ , namely  $\phi = \sum_{i=1}^4 \arg t_i$ , is indicated on the center of each panel ( $a_5 \equiv a_1$ ). The phase is invariant to the choice of the starting cell, although only one such choice is displayed (on the lower left corner). Panels (b-c) indicate the closed path of the type  $c \rightarrow c \rightarrow c \rightarrow d$  corresponds to a chirality  $j_{(cccd)} = +1$  of the total spin current, while panels (e-f) show that the opposite spin chirality  $j_{(dddc)} = -1$  is associated to paths of the type  $c \rightarrow d \rightarrow d \rightarrow d$ . (d) Schematic diagram for the helical state with two counter-propagating edge modes of opposite spins.

### Appendix C: Edge states and symmetry protection

The Bloch Hamiltonian  $\mathcal{H}_0(\mathbf{k})$ , which corresponds to the first two lines of Eq. (A1) or Eq. (A3), describes a system supporting two counter-propagating edge modes of opposite spins (helical state, depicted in Fig. 7d). To see how these spin currents arise, one can analyze elementary plaquettes – displayed in Fig. 7 – and find the hopping paths on which the electrons accumulate non-trivial, spin-dependent phases. There are two of them, as depicted in Fig. 7, ( $c_\sigma \rightarrow c_\sigma \rightarrow c_\sigma \rightarrow d_\sigma$ ) and ( $d_\sigma \rightarrow d_\sigma \rightarrow d_\sigma \rightarrow c_\sigma$ ), and they support spin currents with opposite chiralities –  $j_{(cccd)} = +1$  and  $j_{(dddc)} = -1$ . In the bulk, the two types of spin current have equal weights and cancel out, such that no net spin current exists. However, this symmetry is broken when approaching the boundaries, where one type dominates (arbitrarily chosen in Fig. 7d) and a helical state arises. The counter-propagating states continue to exist on certain edges even when the magnetic fields ( $\mathcal{H}_B$ ) are turned on. In order to prove which symmetry protects them, we introduce a one-dimensional (1D) winding number.

$S$	Equation of $S$	$b, s \rightarrow$	$\mathcal{G}, \mathcal{N} \rightarrow$		$\theta = 0.0$		$\theta = 22.5$		$\theta = 90.0$	
			$D_{2h}, C_{2h}$	$C_{2v}, C_{1h}$	$C_{2h}, C_i$	$C_{1h}, C_1$	$D_{2h}, C_{2h}$	$C_{2v}, C_{1h}$		
$\mathcal{P}$	$-U\mathcal{H}(-k_x, -k_y)^*U^\dagger$	$\sigma_3\tau_1$	✓	✓	✓	✓	✓	✓	✓	✓
$\mathcal{T}$	$+U\mathcal{H}(-k_x, -k_y)^*U^\dagger$	$i\sigma_2\tau_0$	×	×	×	×	×	×	×	×
$\mathcal{C}$	$-U\mathcal{H}(k_x, k_y)U^\dagger$	$\sigma_1\tau_1$	×	×	×	×	×	×	×	×
$\mathcal{I}$	$+U\mathcal{H}(-k_x, -k_y)U^\dagger$	$\sigma_0\tau_3$	✓	×	✓	×	✓	×	✓	×
$\mathcal{R}_2^x$	$+U\mathcal{H}(k_x, -k_y)U^\dagger$	$\sigma_1\tau_3$	×	×	×	×	×	×	✓	×
$\mathcal{R}_2^y$	$+U\mathcal{H}(-k_x, k_y)U^\dagger$	$i\sigma_2\tau_0$	✓	×	×	×	×	×	×	×
$\mathcal{R}_2^z$	$+U\mathcal{H}(-k_x, -k_y)U^\dagger$	$\sigma_3\tau_3$	×	×	×	×	×	×	×	×
$\mathcal{M}_x$	$+U\mathcal{H}(-k_x, k_y)U^\dagger$	$\sigma_1\tau_0$	×	×	×	×	×	×	✓	✓
$\mathcal{M}_y$	$+U\mathcal{H}(k_x, -k_y)U^\dagger$	$i\sigma_2\tau_3$	✓	✓	×	×	×	×	×	×
$\mathcal{M}_z$	$+U\mathcal{H}(k_x, k_y)U^\dagger$	$\sigma_3\tau_0$	×	×	×	×	×	×	×	×
$\mathcal{T} \cdot$										
$\cdot \mathcal{R}_2^x$		$\sigma_3\tau_3$	✓	✓	×	×	×	×	×	×
$\cdot \mathcal{R}_2^y$		$\sigma_0\tau_0$	×	×	×	×	×	×	✓	✓
$\cdot \mathcal{R}_2^z$		$\sigma_1\tau_3$	✓	×	✓	×	×	×	✓	×
$\cdot \mathcal{M}_x$		$\sigma_3\tau_0$	✓	×	×	×	×	×	×	×
$\cdot \mathcal{M}_y$		$\sigma_0\tau_3$	×	×	×	×	×	×	✓	×
$\cdot \mathcal{M}_z$		$\sigma_1\tau_0$	✓	✓	✓	✓	✓	✓	✓	✓
$\mathcal{C} \cdot$										
$\cdot \mathcal{M}_x$		$\sigma_0\tau_1$	✓	×	×	×	×	×	×	×
$\cdot \mathcal{M}_y$		$i\sigma_3\tau_2$	×	×	×	×	×	×	✓	×
$\cdot \mathcal{M}_z$		$i\sigma_2\tau_1$	✓	✓	✓	✓	✓	✓	✓	✓

Table I. Symmetries ( $S$ ) of the bare Hamiltonian  $\mathcal{H}_0$ , on lines: particle-hole antiunitary antisymmetry ( $\mathcal{P}$ ), time-reversal antiunitary symmetry ( $\mathcal{T}$ ), chiral antisymmetry ( $\mathcal{C} = \mathcal{PT}$ ), inversion symmetry ( $\mathcal{I}$ ), two-fold rotation (around  $j$  axis,  $\mathcal{R}_2^j$ ), mirror reflection ( $\mathcal{M}_j$  maps  $x_j \mapsto -x_j$ ), antiunitary symmetries ( $\mathcal{TR}_2^j$  and  $\mathcal{TM}_j$ ) and unitary antisymmetries ( $\mathcal{CM}_j$ ). For each symmetry, the equation of transformation is given, as well as the corresponding representation  $U$  in Hamiltonian space. In the following six columns it is indicated whether the total Hamiltonian  $\mathcal{H} = \mathcal{H}_0 + \mathcal{H}_B + \mathcal{H}_s$  still possesses a certain symmetry, for various values of the parameters  $\mathbf{b} = (b_x, b_y)$  and  $\mathbf{s} = (s_x, s_y)$ ; the corresponding in-plane magnetic fields  $\mathbf{B}_{c,d} = (b_x, \pm b_y, 0)$  and the parameter  $s$  are plotted as arrows of different colors. The parameters for three representative steps of the braiding process are considered,  $2\pi t/T \equiv \theta \in \{0^\circ, 22.5^\circ, 90^\circ\}$ . For each step, two cases are compared: [ $\mathbf{b}$  as indicated and  $\mathbf{s} = (0, 0)$ ] in the former column and [ $\mathbf{b}$  as indicated,  $\mathbf{s}$  as indicated] in the latter column. The point symmetry group of  $\mathcal{H}_0$  is  $D_{4h}$  and is reduced when  $\mathbf{b}, \mathbf{s} \neq 0$ ; the magnetic group of  $\mathcal{H}$  can be written as  $\mathcal{N} \oplus \mathcal{T}(\mathcal{G} - \mathcal{N})$  and, for each column, the groups  $\mathcal{G}$  and  $\mathcal{N}$  are specified.

### 1. 1D winding number

Consider a 2D system with a limited number of unit cells in  $k_\perp$  direction, but with periodic boundary conditions in the other direction  $k_\parallel$ . Provided the bulk Hamiltonian  $\mathcal{H}(\mathbf{k}) \equiv \mathcal{H}(k_x, k_y)$  has an effective chiral symmetry for a certain  $k_\parallel$ ,

$$\{\Gamma, \mathcal{H}(k_\parallel = k_0, k_\perp)\} = 0 \quad \forall k_\perp, \quad (\text{C1})$$

then the relevant topological number is the following 1D winding number [93]:

$$W_{1D}(k_\parallel) = -\frac{1}{4\pi i} \int dk_\perp \text{Tr} \{ \Gamma \mathcal{H}(\mathbf{k})^{-1} \partial_{k_\perp} \mathcal{H}(\mathbf{k}) \}. \quad (\text{C2})$$

The matrix diagonalizing  $\Gamma$  off-diagonalizes the Hamiltonian:

$$U_\Gamma^\dagger \Gamma U_\Gamma = \text{diag}(1, 1, -1, -1) \quad \Rightarrow \quad U_\Gamma^\dagger \mathcal{H}(\mathbf{k}) U_\Gamma = \begin{pmatrix} 0 & h_k \\ h_k^\dagger & 0 \end{pmatrix}, \quad (\text{C3})$$

such that Eq. (C2) can be simplified:

$$W_{1D}(k_\parallel) = \frac{1}{2\pi} \int dk_\perp \partial_{k_\perp} \arg(\det h_k). \quad (\text{C4})$$

This expresses the number of times the phase of  $\det h_k$  winds when the parameter  $k_\perp$  completes a full period.

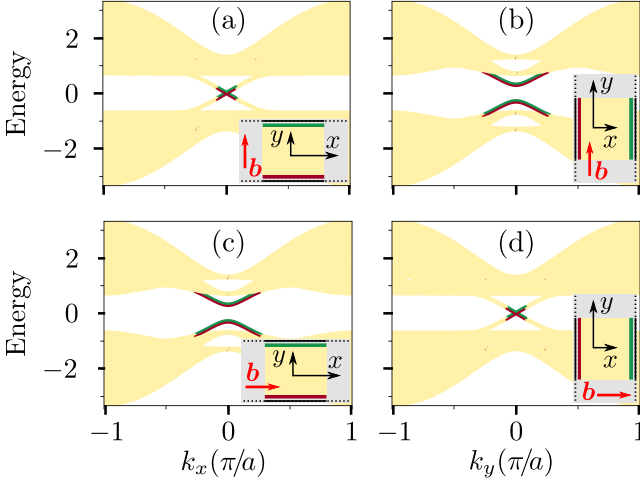


Figure 8. Edge spectra in the presence of magnetic field. As schematically shown in the inset, the parameter  $\mathbf{b} \parallel \hat{y}$  in panels (a-b) and  $\mathbf{b} \parallel \hat{x}$  in panels (c-d). Within each pair of panels, the former illustrates the spectrum of the edges which lie along the  $x$  axis (we call them  $y$  edges), while the latter describes the edges along the  $y$  axis ( $x$  edges). The color of each eigenvalue corresponds to the localization of the respective eigenstate: the boundary modes (dark green and red) can be clearly distinguished from the bulk states (light yellow).

## 2. System infinite in the $x$ -direction

We consider the magnetic field parameter  $\mathbf{b} = (0, b) \parallel \hat{y}$ , for which there are boundary modes which at low energies disperse as  $\pm k_x$  (see Fig. 8a-b) at the  $y$  edges. For our model, the chiral symmetry  $\mathcal{CM}_z$  is present at any momentum  $\mathbf{k}$ :

$$\mathcal{CM}_z : \{ \Gamma, \mathcal{H}(k_x, k_y) \} = 0, \quad \Gamma = \sigma_2 \tau_1, \quad U_\Gamma = \frac{1}{\sqrt{2}} \begin{pmatrix} i & 0 & -i & 0 \\ 0 & i & 0 & -i \\ 0 & 1 & 0 & 1 \\ 1 & 0 & 1 & 0 \end{pmatrix}. \quad (\text{C5})$$

Plugging in  $U_\Gamma$  from Eq. (C5) in Eq. (C3), we obtain the off-diagonal block:

$$h_{\mathbf{k}} = \begin{pmatrix} -\xi_{\mathbf{k}} & b - \Delta_{\mathbf{k}} \\ -b - \Delta_{\mathbf{k}}^* & \xi_{\mathbf{k}} \end{pmatrix} \quad (\text{C6})$$

$$\Rightarrow \det h_{\mathbf{k}} = (b^2 - \xi_{\mathbf{k}}^2 - |\Delta_{\mathbf{k}}|^2) + 2ib \sin k_y,$$

where we denoted  $\Delta_{\mathbf{k}} := \sin k_x - i \sin k_y$ . According to Eq. (C4), the winding number at  $k_x = 0$  is trivial, since:

$$\text{Re} \{ \det h_{(0, k_y)} \} = b^2 - 1 = \text{const}. \quad (\text{C7})$$

Therefore, the boundary modes are *not* protected by the effective chiral antisymmetry  $\mathcal{CM}_z$ . We consider  $\mathcal{CM}_x$  as effective

chiral symmetry at  $k_x = 0$ :

$$\mathcal{CM}_x : \{ \Gamma, \mathcal{H}(k_x = 0, k_y) \} = 0, \quad \Gamma = \sigma_0 \tau_1, \quad U_\Gamma = \frac{1}{\sqrt{2}} \begin{pmatrix} 0 & -1 & 0 & 1 \\ 0 & 1 & 0 & 1 \\ -1 & 0 & 1 & 0 \\ 1 & 0 & 1 & 0 \end{pmatrix}. \quad (\text{C8})$$

This gives a nontrivial winding number as long as  $|b| < 1$ , which means  $\mathcal{CM}_x$  protects the boundary modes (see Fig. 2d):

$$\det h_{(0, k_y)} = \begin{vmatrix} -e^{ik_y} & -ib \\ ib & -e^{ik_y} \end{vmatrix} = e^{2ik_y} - b^2 \quad (\text{C9})$$

$$\stackrel{\text{Eq. (C4)}}{\implies} W_{1\text{D}}(k_x = 0) = 2.$$

The 1D (edge) system has a  $\mathbb{Z}$  topological classification [9, 28, 94] and the topological invariant is precisely the computed winding number, which is equal to the number of states in *one* direction.

## 3. System infinite in the $y$ -direction

The calculations are similar for perpendicular magnetic field  $\mathbf{b} = (b, 0) \parallel \hat{x}$ , for which we have edge states at the  $x$  edges (Fig. 8c-d) which disperse as  $\pm k_y$  at low energies. Using the symmetry  $\mathcal{CM}_z$ , at  $k_y = 0$  we obtain  $\det h_{(k_x, 0)} = b^2 - 1 + 2ib \sin k_x$ , which gives as well a trivial winding number. The edge states are protected by  $\mathcal{CM}_y$  (see Fig. 2e):

$$\mathcal{CM}_y : \{ \Gamma, \mathcal{H}(k_x, k_y = 0) \} = 0, \quad \Gamma = \sigma_3 \tau_2, \quad U_\Gamma = \frac{1}{\sqrt{2}} \begin{pmatrix} 0 & i & 0 & -i \\ 0 & 1 & 0 & 1 \\ -i & 0 & i & 0 \\ 1 & 0 & 1 & 0 \end{pmatrix}. \quad (\text{C10})$$

This gives  $\det h_{(k_x, 0)} = e^{-2ik_x} - b^2$  and thus winding number  $W_{1\text{D}}(k_y = 0) = -2$ .

## Appendix D: Wilson loop operators

We used the nested Wilson loop operator (WLO) to calculate the second-order topological invariants  $\phi_{xy}$  and  $\phi_{yx}$ . This technique was introduced and explained in detail in Refs. [25, 26]; here we only outline the essential steps, which were partly explained in the main text.

### 1. The Wilson loop operator and the Wannier charge centers

One firstly diagonalizes the four-band Bloch Hamiltonian and collects the  $N_{\text{occ}} = 2$  occupied states in a matrix:

$$\mathcal{H} |u_{\mathbf{k}}^j\rangle = E_{\mathbf{k}}^j |u_{\mathbf{k}}^j\rangle, \quad U_{\mathbf{k}} = \left( |u_{\mathbf{k}}^1\rangle \mid |u_{\mathbf{k}}^2\rangle \right). \quad (\text{D1})$$



In this way, the projector to occupied space reads

$$P_k := \sum_{i=1}^{N_{\text{occ}}} |u_k^i\rangle \langle u_k^i| = U_k U_k^\dagger. \quad (\text{D2})$$

For the  $N \times N$  square lattice with lattice constant  $a$ , we analyze the adiabatic evolution of a state  $|u_k^m\rangle$  along a closed path in reciprocal space, with  $k_y$  constant, into a final state  $|u_{k+(2\pi/a,0)}^n\rangle$ . We discretize the path in  $N$  points  $\{\mathbf{k}_j\}$ , with  $\mathbf{k}_j = \mathbf{k} + j\Delta_x$ , where

$$\Delta_x = (\Delta, 0), \quad \Delta = \frac{2\pi}{Na}. \quad (\text{D3})$$

If we iteratively project the initial state until the final state is reached, the amplitude of this parallel transport process can be written as:

$$[\mathcal{W}_{x,k}]_{nm} := \lim_{N \rightarrow \infty} \langle u_{k+(2\pi/a,0)}^n | \prod_{k_i} P_{k_i} |u_k^m\rangle, \quad (\text{D4})$$

where the symbol  $\prod$  stands for ordered product. The unitary matrix  $\mathcal{W}_{x,k}$  represents the WLO in  $x$ -direction; using Eq. (D2), it reads

$$\begin{aligned} \mathcal{W}_{x,k} &= \lim_{N \rightarrow \infty} \underbrace{U_{k+N\Delta_x}^\dagger U_{k+(N-1)\Delta_x}}_{O_{x,k+N\Delta_x}} U_{k+(N-1)\Delta_x}^\dagger \times \dots \\ &\dots \times U_{k+2\Delta_x} \underbrace{U_{k+2\Delta_x}^\dagger U_{k+\Delta_x}}_{O_{x,k+2\Delta_x}} \underbrace{U_{k+\Delta_x}^\dagger U_k}_{O_{x,k+\Delta_x}}, \end{aligned} \quad (\text{D5})$$

where  $O_{x,k}$  denotes an overlap matrix with elements

$$\begin{aligned} [O_{x,k}]_{nm} &:= \langle u_k^n | u_{k-\Delta_x}^m \rangle \\ &= \langle u_k^n | (|u_k^m\rangle - \Delta \partial_{k_x} |u_k^m\rangle) + O(\Delta^2) \\ &= \langle u_k^n | u_k^m \rangle - \Delta \langle u_k^n | \partial_{k_x} |u_k^m\rangle + O(\Delta^2). \\ &= \delta_{nm} + i\Delta [\mathcal{A}_k^x]_{nm} + O(\Delta^2). \end{aligned} \quad (\text{D6})$$

In the last equality, we recognized the matrix element  $nm$  of  $\mathcal{A}_k^x$ , the  $x$  component of the Berry connection constructed with the occupied Bloch eigenfunctions. Combining the last two equations, we get:

$$\begin{aligned} \mathcal{W}_{x,k} &= \lim_{N \rightarrow \infty} \prod_j O_{x,k+j\Delta_x} = \lim_{N \rightarrow \infty} \prod_j (\mathbb{1} + i\Delta \mathcal{A}_{k+j\Delta_x}^x) \\ &= \overline{\text{exp}} \left( i \oint_{q_y=k_y} dq_x \mathcal{A}_q^x \right). \end{aligned} \quad (\text{D7})$$

The last equality is presented in the main text [Eq. (3)], however, the first equality of Eq. (D7) is used in practice to compute the WLO, with a finite number  $N$  of  $\mathbf{k}$  points. The spectrum of the WLO is found by solving

$$\mathcal{W}_{x,k} |\bar{x}_n(\mathbf{k})\rangle = \lambda_x^n(k_y) |\bar{x}_n(\mathbf{k})\rangle. \quad (\text{D8})$$

In the main text, the connection between the  $N_{\text{occ}} \times N_{\text{occ}}$  unitary operator  $\mathcal{W}_{x,k}$  and the physics at the  $x$  edge was mentioned. Here, we emphasize additionally that the eigenvalues

$\lambda_x^n$  are related to the surface charge polarization [95, 96], since their phases are proportional to the Wannier charge centers (WCCs)  $\bar{x}_n$ :

$$\lambda_x^n(k_y) =: \exp(i\phi_x^n(k_y)) = \exp\left(2\pi i \frac{\bar{x}_n(k_y)}{a}\right). \quad (\text{D9})$$

Here, the quantity  $\bar{x}_n$  is defined mod  $a$ , as the center of the  $n$ -th hybrid Wannier function, which is maximally localized in  $x$ -direction and Bloch-like in  $k_y$ -direction [72, 97]. Typical shapes for the flow of WCCs  $\bar{x}_n$  are displayed in Fig. 3a and Fig. 3c.

*Symmetry protection of the WCC crossings.* Let's consider first  $\mathbf{s} = (0, 0)$  and  $\mathbf{b} = (-0.3, 0)$ , for which the WCCs  $\bar{x}_j(k_y)$  anticross, as shown in Fig. 3c. The discussion around Eq. (C10) proved that the edge states were protected by  $\mathcal{C}\mathcal{M}_y$  symmetry, which arose from the crystalline symmetry  $\mathcal{R}_{2x}$  (multiplied with the effective 2D chiral symmetry  $\mathcal{C}\mathcal{M}_z$ , see Table I). This was the only crystalline symmetry of the 1D system, however the bulk (and therefore the WCCs, too) possesses two additional symmetries: mirror reflection  $\mathcal{M}_x$  and inversion  $\mathcal{I}$ . The anticrossing of the WCCs is, in fact, owed to inversion symmetry  $\mathcal{I}$ , and this feature survives even when  $\mathbf{b} \nparallel \hat{x}$ , since the magnetic field pseudovectors  $\mathbf{B}_{c,d}$  are invariant to inversion. If we have additionally  $\mathbf{s} = (0, 0.3)$  [while  $\mathbf{b} = (-0.3, 0)$ ], then only  $\mathcal{M}_x$  survives in the bulk and thus both the 1D ribbon and the WCCs are gapped – see Fig. 3a.

We remark that  $\bar{x}(k_y)$  are fully gapped by  $\mathcal{H}_s = s_y \cos k_y \sigma_1 \tau_1$ , but this only removes the anticrossing  $\bar{y}(\pi)$ ; however, the crossing  $\bar{y}(0)$  is *not* protected by any symmetry and can be annihilated if  $s_0 \sigma_1 \tau_1$  is added to  $\mathcal{H}_s$ , where  $s_0$  is infinitesimally small (Fig. 3b).

## 2. The nested Wilson loop operator

If one can separate two sets of Wannier bands which do not touch over the entire range  $k_y \in [0, 2\pi/a]$ , one set can be conventionally called the "occupied" Wannier subspace and can be topologically characterized separately. The nested WLO [25, 26] can be computed using the "occupied" kets (only one in our model), by firstly constructing the linear combinations

$$|w_{x,k}^n\rangle = \sum_{j=1}^{N_{\text{occ}}} [\bar{x}_n(\mathbf{k})]^j |u_k^j\rangle, \quad n \in \{1, \dots, N_{\text{occ}}/2\}. \quad (\text{D10})$$

The overlap matrices of these wavefunctions are, similarly to Eq. (D6),

$$[\tilde{O}_{xy,k}]_{nm} := \langle w_k^n | w_{k-\Delta_y}^m \rangle = \delta_{nm} + i\Delta [\tilde{\mathcal{A}}_k^{xy}]_{nm} + O(\Delta^2), \quad (\text{D11})$$

where  $\Delta_y = (0, \Delta)$  and the new Berry connection  $\tilde{\mathcal{A}}_k^{xy}$  has elements  $[\tilde{\mathcal{A}}_k^{xy}]_{nm} = i \langle w_{x,k}^n | \partial_{k_y} |w_{x,k}^m\rangle$ . The corresponding WLO follows Eq. (D7),

$$\widetilde{\mathcal{W}}_{xy,k_x} = \lim_{N \rightarrow \infty} \prod_j \tilde{O}_{xy,k+j\Delta_y} = \overline{\text{exp}} \left( i \oint_{q_x=k_x} dq_y \tilde{\mathcal{A}}_q^{xy} \right), \quad (\text{D12})$$

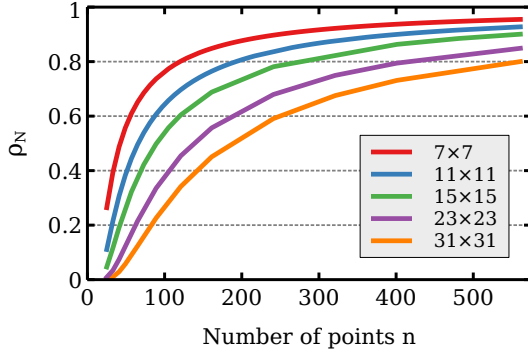


Figure 9. Non-unitarity  $\rho_N$  of the WLO in  $t$ -space, as a function of the number of numerical steps, for various material sample sizes  $N \times N$ . In Eq. (E1) we defined  $\rho_N(n)$  for either of the two MCSs (it has the same behavior for both A and B).

which appeared as well in the main text [Eq. (4)]. The corner topological invariant reads

$$\phi_{xy} = \frac{1}{N} \sum_{k_x} \arg \det \widetilde{\mathcal{W}}_{xy,k_x} = \frac{a}{2\pi} \int_0^{2\pi/a} dk_x \arg \det \widetilde{\mathcal{W}}_{xy,k_x}. \quad (\text{D13})$$

In our model,  $N_{\text{occ}} = 2$  and  $\widetilde{\mathcal{W}}_{xy,k_x}$  is, in fact, a complex number (not a matrix), such that no “det” is needed in Eq. (5) and the topological invariant is encoded by a single Wannier band. The topological invariant  $\phi_{yx}$  is computed in a similar fashion (formally one swaps  $x \leftrightarrow y$ ). It is worth mentioning that  $\phi_{xy}$  and  $\phi_{yx}$  are, in fact, the corner polarizations [25, 26] (up to a factor  $2\pi/e$ , where  $e$  is the electron charge).

## Appendix E: Calculation of statistical phase

We computed the statistical phase as a Berry phase in  $t$ -space – see Eq. (D7) for the Brillouin zone WLO. We evaluated the corresponding WLO by making a discretization of the  $t$ -space in  $n$  steps:

$$\rho_N(n) \exp(i\Phi_\alpha) = \prod_{j=1}^n \langle \psi_\alpha(t_{j-1}) | \psi_\alpha(t_j) \rangle, \quad t_j = j \frac{T}{n}. \quad (\text{E1})$$

Here  $\alpha \in \{A, B\}$  refers to either of the two MCSs and the factor  $\rho_N(n)$  – independent of  $\alpha$ , but depending on the system size  $N$  and on the density of the time mesh  $n$  – has been introduced to account for the non-unitarity of the Wilson loop product on the right-hand side (note that  $N$  is finite, thermodynamic limit  $N \rightarrow \infty$  is not assumed). The periodic boundary condition  $\mathcal{H}^{(t=0)} = \mathcal{H}^{(t=T)}$  implies  $|\psi_\alpha(t_0)\rangle \equiv |\psi_\alpha(t_n)\rangle$ .

In Fig. 9 we plot  $\rho_N(n)$  for several system sizes. Not surprisingly, it increases when the number of steps  $n$  increases and it would reach unity if the braiding speed went to zero ( $\lim_{n \rightarrow \infty} \rho_N(n) = 1$ ). On the other hand, for a certain  $n$ , it decreases when the system size increases; physically, this means the speed of the braiding process should be lower for larger systems because the phase space where the MCSs live is larger.

Although at  $t = T/2$  an exchange of the MCSs  $A \leftrightarrow B$  is achieved (shown in Fig. 4), the wavefunction A at  $t = 0$  has small overlap with the wavefunction B at  $t = T/2$  because the Hamiltonians are different and do not commute ( $\nexists U$  such that  $\mathcal{H}^{(t=T/2)} = U\mathcal{H}^{(t=0)}U^\dagger$ ). Consequently, within the current model the Majorana exchange statistics cannot be observed.

- 
- [1] C. L. Kane and E. J. Mele, Phys. Rev. Lett. **95**, 146802 (2005).
  - [2] B. A. Bernevig, T. L. Hughes, and S.-C. Zhang, Science **314**, 1757 (2006).
  - [3] L. Fu and C. L. Kane, Phys. Rev. B **74**, 195312 (2006).
  - [4] L. Fu, C. L. Kane, and E. J. Mele, Phys. Rev. Lett. **98**, 106803 (2007).
  - [5] L. Fu and C. L. Kane, Phys. Rev. B **76**, 045302 (2007).
  - [6] M. Z. Hasan and C. L. Kane, Rev. Mod. Phys. **82**, 3045 (2010).
  - [7] X.-L. Qi and S.-C. Zhang, Rev. Mod. Phys. **83**, 1057 (2011).
  - [8] C.-K. Chiu, J. C. Y. Teo, A. P. Schnyder, and S. Ryu, Rev. Mod. Phys. **88**, 035005 (2016).
  - [9] A. P. Schnyder, S. Ryu, A. Furusaki, and A. W. W. Ludwig, Phys. Rev. B **78**, 195125 (2008).
  - [10] A. P. Schnyder, S. Ryu, A. Furusaki, A. W. W. Ludwig, V. Lebedev, and M. Feigel'man, AIP Conf. Proc. **1134**, 10 (2009).
  - [11] A. Kitaev, V. Lebedev, and M. Feigel'man, AIP Conf. Proc. **1134**, 22 (2009).
  - [12] L. Fu, Phys. Rev. Lett. **106**, 106802 (2011).
  - [13] T. H. Hsieh, H. Lin, J. Liu, W. Duan, A. Bansil, and L. Fu, Nat. Commun. **3**, 982 (2012).
  - [14] R.-J. Slager, A. Mesaros, V. Juričić, and J. Zaanen, Nat. Phys. **9**, 98 (2012).
  - [15] C.-K. Chiu, H. Yao, and S. Ryu, Phys. Rev. B **88**, 075142 (2013).
  - [16] T. Morimoto and A. Furusaki, Phys. Rev. B **88**, 125129 (2013).
  - [17] K. Shiozaki and M. Sato, Phys. Rev. B **90**, 165114 (2014).
  - [18] W. A. Benalcazar, J. C. Y. Teo, and T. L. Hughes, Phys. Rev. B **89**, 224503 (2014).
  - [19] A. Alexandradinata, C. Fang, M. J. Gilbert, and B. A. Bernevig, Phys. Rev. Lett. **113**, 116403 (2014).
  - [20] K. Shiozaki, M. Sato, and K. Gomi, Phys. Rev. B **93**, 195413 (2016).
  - [21] J. Kruthoff, J. de Boer, J. van Wezel, C. L. Kane, and R.-J. Slager, Phys. Rev. X **7**, 041069 (2017).
  - [22] K. Shiozaki, M. Sato, and K. Gomi, Phys. Rev. B **95**, 235425 (2017).
  - [23] R. Thorngren and D. V. Else, Phys. Rev. X **8**, 011040 (2018).
  - [24] E. Khalaf, H. C. Po, A. Vishwanath, and H. Watanabe, Phys. Rev. X **8**, 031070 (2018).
  - [25] W. A. Benalcazar, B. A. Bernevig, and T. L. Hughes, Science **357**, 61 (2017).
  - [26] W. A. Benalcazar, B. A. Bernevig, and T. L. Hughes, Phys. Rev. B **96**, 245115 (2017).
  - [27] Z. Song, Z. Fang, and C. Fang, Phys. Rev. Lett. **119**, 246402 (2017).
  - [28] M. Geier, L. Trifunovic, M. Hoskam, and P. W. Brouwer, Phys. Rev. B **97**, 205135 (2018).
  - [29] F. Schindler, A. M. Cook, M. G. Vergniory, Z. Wang, S. S. P. Parkin, B. A. Bernevig, and T. Neupert, Sci. Adv. **4**, eaat0346 (2018).

- [30] C. W. Peterson, W. A. Benalcazar, T. L. Hughes, and G. Bahl, *Nature* **555**, 346 (2018).
- [31] E. Khalaf, *Phys. Rev. B* **97**, 205136 (2018).
- [32] M. Ezawa, *Phys. Rev. Lett.* **120**, 026801 (2018).
- [33] G. van Miert and C. Ortix, *Phys. Rev. B* **98**, 081110(R) (2018).
- [34] C.-H. Hsu, P. Stano, J. Klinovaja, and D. Loss, *Phys. Rev. Lett.* **121**, 196801 (2018).
- [35] S. Franca, J. van den Brink, and I. C. Fulga, *Phys. Rev. B* **98**, 201114(R) (2018).
- [36] J. Ahn and B.-J. Yang, *ArXiv e-prints* (2018), 1810.05363v2.
- [37] B. Huang and W. V. Liu, *ArXiv e-prints* (2018), 1811.00555.
- [38] D. Călugăru, V. Juričić, and B. Roy, *Phys. Rev. B* **99**, 041301(R) (2019).
- [39] A. Agarwala, V. Juricic, and B. Roy, *ArXiv e-prints* (2019), 1902.00507.
- [40] S. A. A. Ghorashi, X. Hu, T. L. Hughes, and E. Rossi, *ArXiv e-prints* (2019), 1901.07579.
- [41] A. Y. Kitaev, *Phys. Usp.* **44**, 131 (2001).
- [42] A. Kitaev, *Ann. Phys.* **321**, 2 (2006).
- [43] C. Nayak, S. H. Simon, A. Stern, M. Freedman, and S. DasSarma, *Rev. Mod. Phys.* **80**, 1083 (2008).
- [44] J. Alicea, *Rep. Prog. Phys.* **75**, 076501 (2012).
- [45] S. D. Sarma, M. Freedman, and C. Nayak, *npj Quantum Inf.* **1**, 15001 (2015).
- [46] L. Fidkowski and A. Kitaev, *Phys. Rev. B* **81**, 134509 (2010).
- [47] L. Fidkowski and A. Kitaev, *Phys. Rev. B* **83**, 075103 (2011).
- [48] R. M. Lutchyn, J. D. Sau, and S. DasSarma, *Phys. Rev. Lett.* **105**, 077001 (2010).
- [49] Y. Oreg, G. Refael, and F. von Oppen, *Phys. Rev. Lett.* **105**, 177002 (2010).
- [50] V. Mourik, K. Zuo, S. M. Frolov, S. R. Plissard, E. P. A. M. Bakkers, and L. P. Kouwenhoven, *Science* **336**, 1003 (2012).
- [51] A. Das, Y. Ronen, Y. Most, Y. Oreg, M. Heiblum, and H. Shtrikman, *Nat. Phys.* **8**, 887 (2012).
- [52] M. T. Deng, C. L. Yu, G. Y. Huang, M. Larsson, P. Caroff, and H. Q. Xu, *Nano Lett.* **12**, 6414 (2012).
- [53] A. D. K. Finck, D. J. VanHarlingen, P. K. Mohseni, K. Jung, and X. Li, *Phys. Rev. Lett.* **110**, 126406 (2013).
- [54] H. O. H. Churchill, V. Fatemi, K. Grove-Rasmussen, M. T. Deng, P. Caroff, H. Q. Xu, and C. M. Marcus, *Phys. Rev. B* **87**, 241401(R) (2013).
- [55] M. T. Deng, S. Vaitiekėnas, E. B. Hansen, J. Danon, M. Leijnse, K. Flensberg, J. Nygård, P. Krogstrup, and C. M. Marcus, *Science* **354**, 1557 (2016).
- [56] J. Alicea, Y. Oreg, G. Refael, F. von Oppen, and M. P. A. Fisher, *Nat. Phys.* **7**, 412 (2011).
- [57] B. van Heck, A. R. Akhmerov, F. Hassler, M. Burrello, and C. W. J. Beenakker, *New J. Phys.* **14**, 035019 (2012).
- [58] X. Zhu, *Phys. Rev. B* **97**, 205134 (2018).
- [59] Z. Yan, F. Song, and Z. Wang, *Phys. Rev. Lett.* **121**, 096803 (2018).
- [60] Q. Wang, C.-C. Liu, Y.-M. Lu, and F. Zhang, *Phys. Rev. Lett.* **121**, 186801 (2018).
- [61] T. Liu, J. J. He, and F. Nori, *Phys. Rev. B* **98**, 245413 (2018).
- [62] C. Schrade and L. Fu, *ArXiv e-prints* (2018), 1807.06620.
- [63] Here, the set  $(D_{2h} - C_{2h})$  represents the relative complement of  $C_{2h}$  with respect to  $D_{2h}$ . It contains the elements of  $D_{2h}$  which are not part of  $C_{2h}$  and it is *not* a group by itself.
- [64] M. Ezawa, *Phys. Rev. Lett.* **121**, 116801 (2018).
- [65] S. Coh and D. Vanderbilt, *Phys. Rev. Lett.* **102**, 107603 (2009).
- [66] R. Yu, X. L. Qi, A. Bernevig, Z. Fang, and X. Dai, *Phys. Rev. B* **84**, 075119 (2011).
- [67] X.-L. Qi, *Phys. Rev. Lett.* **107**, 126803 (2011).
- [68] M. V. Berry, *Proc. R. Soc. London, Ser. A* **392**, 45 (1984).
- [69] F. Wilczek and A. Zee, *Phys. Rev. Lett.* **52**, 2111 (1984).
- [70] L. Fidkowski, T. S. Jackson, and I. Klich, *Phys. Rev. Lett.* **107**, 036601 (2011).
- [71] M. Taherinejad, K. F. Garrity, and D. Vanderbilt, *Phys. Rev. B* **89**, 115102 (2014).
- [72] A. A. Soluyanov and D. Vanderbilt, *Phys. Rev. B* **83**, 035108 (2011).
- [73] A. A. Soluyanov and D. Vanderbilt, *Phys. Rev. B* **83**, 235401 (2011).
- [74] A. Alexandradinata, X. Dai, and B. A. Bernevig, *Phys. Rev. B* **89**, 155114 (2014).
- [75] A. Alexandradinata and B. A. Bernevig, *Phys. Rev. B* **93**, 205104 (2016).
- [76] D. Gresch, G. Autès, O. V. Yazyev, M. Troyer, D. Vanderbilt, B. A. Bernevig, and A. A. Soluyanov, *Phys. Rev. B* **95**, 075146 (2017).
- [77] The Hermitian edge Hamiltonian  $H_{\text{edge}}$  could be related to the *unitary* WLO through the mapping  $\mathcal{W}_{x,k} = \exp(iH_{\text{edge}})$ .
- [78] B.-Y. Xie, H.-F. Wang, H.-X. Wang, X.-Y. Zhu, J.-H. Jiang, M.-H. Lu, and Y.-F. Chen, *Phys. Rev. B* **98**, 205147 (2018).
- [79] If we considered  $\mathbf{b} = (0, -0.3)$  and  $\mathbf{s} = (0.3, 0)$ , the opposite would be valid:  $(\phi_{xy}, \phi_{yx}) = (0, \pi)$ .
- [80] L. Cheng, L. Wei, H. Liang, Y. Yan, G. Cheng, M. Lv, T. Lin, T. Kang, G. Yu, J. Chu, Z. Zhang, and C. Zeng, *Nano Lett.* **17**, 6534 (2017).
- [81] V. Sih and D. D. Awschalom, *J. Appl. Phys.* **101**, 081710 (2007).
- [82] G. Jotzu, M. Messer, R. Desbuquois, M. Lebrat, T. Uehlinger, D. Greif, and T. Esslinger, *Nature* **515**, 237 (2014).
- [83] X.-J. Liu, K. T. Law, and T. K. Ng, *Phys. Rev. Lett.* **112**, 086401 (2014).
- [84] X.-T. Xu, C.-R. Yi, B.-Z. Wang, W. Sun, Y. Deng, X.-J. Liu, S. Chen, and J.-W. Pan, *Sci. Bull.* **63**, 1464 (2018).
- [85] M. Atala, M. Aidelsburger, J. T. Barreiro, D. Abanin, T. Kitagawa, E. Demler, and I. Bloch, *Nat. Phys.* **9**, 795 (2013).
- [86] L. Duca, T. Li, M. Reitter, I. Bloch, M. Schleier-Smith, and U. Schneider, *Science* **347**, 288 (2014).
- [87] N. Flaschner, B. S. Rem, M. Tarnowski, D. Vogel, D.-S. Luhmann, K. Sengstock, and C. Weitenberg, *Science* **352**, 1091 (2016).
- [88] T. Li, L. Duca, M. Reitter, F. Grusdt, E. Demler, M. Endres, M. Schleier-Smith, I. Bloch, and U. Schneider, *Science* **352**, 1094 (2016).
- [89] N. Goldman, G. Jotzu, M. Messer, F. Gorg, R. Desbuquois, and T. Esslinger, *Phys. Rev. A* **94**, 043611 (2016).
- [90] M. Mancini, G. Pagano, G. Cappellini, L. Livi, M. Rider, J. Catani, C. Sias, P. Zoller, M. Inguscio, M. Dalmonte, and L. Fallani, *Science* **349**, 1510 (2015).
- [91] B. K. Stuhl, H.-I. Lu, L. M. Ayccock, D. Genkina, and I. B. Spielman, *Science* **349**, 1514 (2015).
- [92] A. V. Shubnikov and N. V. Belov, *Colored symmetry*, edited by W. Holser (Oxford, Pergamon Press, 1964).
- [93] M. Sato, Y. Tanaka, K. Yada, and T. Yokoyama, *Phys. Rev. B* **83**, 224511 (2011).
- [94] J. C. Y. Teo and C. L. Kane, *Phys. Rev. B* **82**, 115120 (2010).
- [95] E. I. Blount, in *Solid State Physics* (Elsevier, 1962) pp. 305–373.
- [96] R. D. King-Smith and D. Vanderbilt, *Phys. Rev. B* **47**, 1651 (1993).
- [97] N. Marzari and D. Vanderbilt, *Phys. Rev. B* **56**, 12847 (1997).